

Neutron ghost imaging

Andrew M. Kingston  and Glenn R. Myers 

Department of Applied Mathematics, Research School of Physics and Engineering, The Australian National University, Canberra, Acton 2601, Australia

and CTLab: National Laboratory for Micro Computed-Tomography, Advanced Imaging Precinct, The Australian National University, Canberra, Acton 2601, Australia

Daniele Pelliccia 

Instruments & Data Tools Pty. Ltd., Victoria 3178, Australia

Filomena Salvemini , Joseph J. Bevitt, and Ulf Garbe 

Australian Centre for Neutron Scattering, Australian Nuclear Science and Technology Organisation, New Illawarra Road, Lucas Heights, New South Wales 2234, Australia

David M. Paganin

School of Physics and Astronomy, Monash University, Victoria 3800, Australia



(Received 28 November 2019; accepted 17 March 2020; published 18 May 2020)

Ghost imaging is demonstrated using a polyenergetic reactor source of thermal neutrons. This enables position resolution to be incorporated into a variety of neutron instruments that are not position resolving. Such a proof of concept enables several further applications. For example, in an imaging context, neutron ghost imaging can be beneficial for dose reduction and resolution enhancement. We explore the principle of resolution enhancement by employing a variant of the method in which each pixel of a position-sensitive detector is regarded as an independent bucket detector; a neutron ghost image is then computed for each pixel. We demonstrate the principle that this parallel form of neutron ghost imaging can significantly increase the spatial resolution of a pixelated detector such as a CCD or CMOS camera. Further applications and extensions of our neutron ghost-imaging protocol are discussed. These include neutron ghost tomography, neutron ghost microscopy, dark-field neutron ghost imaging, and isotope-resolved color neutron ghost imaging via prompt-gamma-ray bucket detection.

DOI: [10.1103/PhysRevA.101.053844](https://doi.org/10.1103/PhysRevA.101.053844)

I. INTRODUCTION

Ghost imaging (GI) was originally developed in the context of visible-light quantum optics [1–4]. The *spooky* action at a distance of quantum entangled photons (initially thought to be required for the technique) gave rise to its name. It was later determined that only the correlation property of the photons is required [5,6] and classical forms of GI arose [7]. GI has the ability to enhance the signal-to-noise ratio (SNR) [8], reduce dose given significant *a posteriori* knowledge of the object [9], and provide subwavelength resolution [10]. The *classical* GI variant works as follows [see Fig. 1(a) for a depiction]: An ensemble of spatially random illuminating patterns strikes a beam splitter Q . The intensity distribution of the secondary (reflected) beam is recorded using a pixelated detector P ; the primary beam passes through a sample of interest and then has its total transmitted intensity recorded using a large single-pixel detector, called a “bucket,” B . While P records images that contain no information about the object, imaging quanta that are registered by B have passed through the object, but are never measured with positional information. Neither of the signals at P or B individually contain position-sensitive information regarding the sample; however, a ghost image of the sample may be reconstructed via intensity-intensity

correlations between the two signals [9,11]. This may be viewed as a parallel version of the intensity-intensity correlation experiment of Hanbury Brown and Twiss [12–14].

A variant of classical ghost imaging known as *computational* ghost imaging (CGI) was later developed where the spatially random illumination patterns are predetermined [15] [see Fig. 1(b)]. Here the mask need not be measured during the ghost-imaging procedure since it is either known (and associated illumination patterns simulated), controlled (e.g., employing digital micromirror devices), or premeasured [as exemplified in Fig. 1(b-i)]. With the illumination patterns known, bucket signals may then be measured, as shown in Fig. 1(b-ii). Here, the resolution of the final computational ghost image is limited to the resolution at which the mask is characterized [7,15]. CGI is extremely similar to the single-pixel camera concept [16,17]; however, in CGI, the illumination is patterned rather than the detector. This is an important distinction when considering dark-field imaging techniques as well as minimizing dose incident on the object. Further information, regarding all of the points mentioned in the present paragraph, is given in several review articles [7,18,19].

Moving beyond the domain of visible-light optics, ghost imaging has now been realized using hard x rays [20–22],

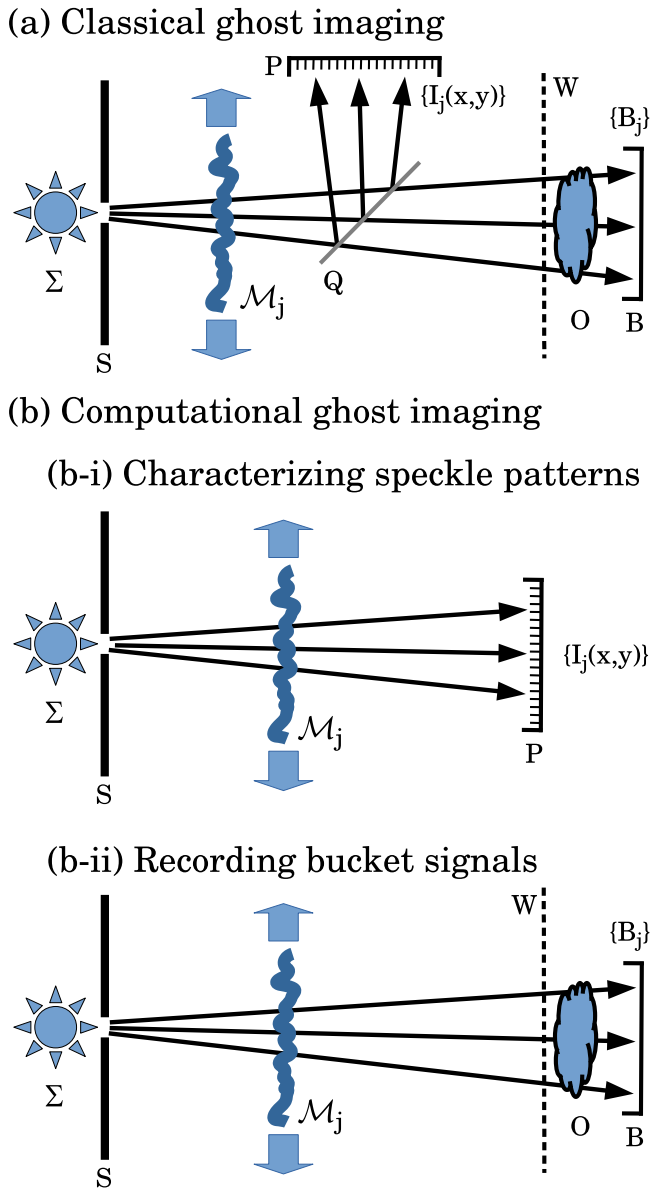


FIG. 1. Setup for variants of classical transmission ghost imaging. Imaging quanta (e.g., visible-light photons, neutrons, x rays, gamma rays, etc.) from a source Σ pass through a slit S before traversing a spatially random mask \mathcal{M}_j to give a spatially random image $I_j(x, y)$ recorded by a position-sensitive detector P . The total transmission of this j^{th} speckled illumination through sample O , B_j , is recorded using a position-insensitive detector (“bucket” detector) B . (a) A beam splitter Q is employed for simultaneous acquisition of $I_j(x, y)$ and B_j . (b) An example of *computational ghost imaging* that performs sequential acquisition of $I_j(x, y)$ and B_j . (b-i) The ensemble of random intensity maps $\{I_j(x, y)\}$, where $j = 1, 2, \dots, N$, given N different mask positions, is prerecorded. (b-ii) The corresponding ensemble of bucket signals $\{B_j\}$ is then measured. Note that the entrance surface W of the sample coincides with the distance to the plane occupied by P , in both variants illustrated above.

ultracold-atom beams [23,24], and electrons [25]. In this paper, we first demonstrate that GI can be achieved with neutrons and then explore potential future neutron ghost-imaging (NGI) applications. NGI may be viewed as a spatial-

multiplexing extension of the temporal-multiplexing approach to random-chopper or random-spin-flipper time-of-flight neutron spectroscopy [26–31]. A parallel also exists between the NGI work presented in this paper and the recent proposal by Chen and Han [32] for Fourier-transform neutron ghost imaging utilizing fermionic antibunching.

As a probe, neutrons have many properties in common with hard x rays. Being poorly interacting uncharged particles with similar wavelengths, they can provide many similar transmission, scatter, and reflection capabilities. However, neutrons possess quite complementary contrast mechanisms [33,34]. Neutron imaging is currently advancing rapidly; however, many challenges still remain to be solved: (i) Neutrons are ionizing radiation (often causing nuclear activation of samples) and dose must be limited. (ii) Nuclear-reactor and spallation neutron sources only provide limited neutron flux; an experiment must work with a broad spectrum for maximum flux, or accept extremely low flux if monochromatic conditions are required. (iii) It is difficult to focus polychromatic neutrons; this combined with (ii) complicates the development of scanning-probe techniques. (iv) High-resolution neutron microscopy is notoriously difficult (conventional imaging is currently limited to a resolution of about $10 \mu\text{m}$ [35]), with research being conducted into efficient scintillator materials [36] to reduce scintillator thickness (and thus increase spatial resolution) without sacrificing detected neutron flux. Neutron microscopy through compound refractive lenses is also being explored [37–40] and, while promising, does not yet provide resolutions matching conventional imaging.

Motivation and context for our paper is given by the possibility that future researchers will be enabled by GI to address some of the above limitations and extend current capabilities of neutron probe techniques. In particular, our work has the following longer-term goals in view:

(i) Once the spatially random mask \mathcal{M} has been accurately characterized (or is known *a priori*), GI requires only a bucket detector and can enable imaging capabilities to be added to a variety of neutron instruments that are not position resolving. The suite of existing neutron-imaging methods [33,41] may, in the future, be usefully extended via the addition of neutron ghost imaging and tomography. Examples include instruments for triple-axis neutron spectrometry, small-angle neutron scattering, time-of-flight spectrometry, strain scanning and reflectometry. Such an augmentation would appear to be reasonably straightforward.

(ii) GI provides the ability to yield isotope-resolved images via prompt-gamma-ray bucket detection. A dark-field version of the method is also possible, in which the bucket detector records neutrons scattered through an appreciable angle.

(iii) GI is a computational imaging technique and, given sufficient *a posteriori* knowledge of a sample, fewer measurements are required (cf. conventional imaging) to image the sample, thus providing a route to dose reduction (and, where appropriate, reduction of sample damage or activation). This is also true for tomographic variants of GI, with the experimental proof of concept for x-ray ghost tomography having recently been achieved [42,43].

(iv) GI gives a simple and readily implementable route to high-resolution neutron microscopy by enabling the resolving power of a given position-sensitive neutron detector to be

significantly increased. Each pixel becomes a bucket detector used to form a ghost image up to the resolution to which the speckle generating mask is known.

In what follows, we present a simple scheme to utilize an existing tomographic imaging configuration in order to demonstrate computational ghost imaging with neutrons. We then explore one of the above potential applications: a parallelized form of the neutron ghost-imaging technique that illustrates the principle that one may achieve high-resolution microscopy by ghost imaging. In this parallelized form, a contiguous pixelated array of bucket detectors is used to reconstruct a contiguous array of neutron ghost images. The remaining applications are considered in more detail in the discussion.

We now elaborate on the concept of parallelized neutron ghost imaging: Given no knowledge of the sample, an ensemble of GI measurements using N orthogonal speckle patterns can increase the resolution of the 1×1 pixel *bucket* detector to a $\sqrt{N} \times \sqrt{N}$ pixel array spanning the same field of view (FOV), i.e., a zoom factor of \sqrt{N} . (Note that here we assume that the speckle patterns possess the required feature resolution.) If one thinks of each of the M pixels in a conventional imaging detector as a *bucket*, then, by using GI techniques, a set of N orthogonal speckle patterns can increase the resolution of this contiguous $\sqrt{M} \times \sqrt{M}$ array of *bucket* pixels to a $\sqrt{MN} \times \sqrt{MN}$ pixel array with the same FOV. Note that the equivalent GI resolution from a single bucket detector would require MN orthogonal speckle patterns to achieve the same result. This principle has the potential to enable neutron microscopy and even ultramicroscopy while still employing thick, cheap scintillator screens with a high stopping power.

We close this introduction by outlining the remainder of the paper. Section II reviews some of the general background for ghost imaging. This section also establishes a protocol for neutron ghost imaging. Section III describes the experimental methods used to obtain the results in Sec. IV. Computational neutron ghost imaging and its parallelized form are separately treated in Secs. IV B and IV C, respectively. We discuss some implications of our results in Sec. V, followed by some potential future applications in Sec. VI. We conclude with a summary in Sec. VII.

II. BACKGROUND

Here we outline key aspects of computational neutron ghost imaging. We draw on generic background developed in visible-light studies: see, e.g., the previously cited review articles [7,18,19] and references therein. We also draw on protocols developed for ghost imaging using hard x rays [20–22,42–45]. This latter link arises from the fact that the connection between neutron ghost imaging and hard x-ray ghost imaging is necessarily close since (i) both are highly penetrating illumination probes, for samples opaque to visible light, electrons, atomic beams, molecular beams, etc.; (ii) thermal neutrons have a de Broglie wavelength of the order of 10^{-10} m, similar to the wavelength of hard x rays; (iii) while neutron sources are typically significantly less brilliant than corresponding x-ray sources, source sizes can be made comparable, and experimental imaging geometries often have similar spatial dimensions; (iv) both x-ray and

neutron optics often employ optical elements that are similar in nature—e.g., crystal beam splitters, compound refractive lenses, scintillator-coupled position-sensitive detectors, etc.—and are qualitatively different to their visible-light counterparts; and (v) efficient high-resolution spatial light modulators, which are readily available for optical studies with visible light and form a key component of many computational ghost-imaging setups, have yet to be realized for both neutron and x-ray optics.

Consider an ensemble of N spatially random intensity distributions $\{I_j(x, y)\}$, where $j = 1, \dots, N$ and (x, y) are transverse Cartesian coordinates in planes orthogonal to an optical axis z . We speak of these distributions as “speckle” maps, in a more general usage of the term than that which equates “speckle” with “fully developed coherent speckle.” The ensemble of random intensity maps may be generated as shown in Fig. 2(a). Here, a spatially uniform beam of z -directed neutrons illuminates a speckle-generating mask composed of a cylinder that comprises either (i) a thin [46] cylindrical shell whose surface is coated with a spatially random distribution of highly-neutron-absorbent particles such as gadolinium oxysulfide (Gadox) powder, or (ii) a pair of thin cylindrical shells between which is contained a spatially random highly-neutron-absorbent material such as randomly packed steel ball bearings or sodium chloride grains. Rotating this illuminated mask through a series of azimuthal orientations θ about its axis A , as well as displacing it parallel to A , generates the required ensemble $\{I_j(x, y)\}$. This ensemble may be (i) measured once and for all using the position-sensitive detector P or (ii) may be computationally inferred if the three-dimensional (3D) structure of the mask has been accurately characterized (e.g., using neutron or x-ray tomography) and the properties of the illuminating neutron beam (divergence, spectrum, etc.) are well known and stable. The speckles should have high contrast κ since the SNR of the resulting ghost image is proportional to κ [47]. Assume that the mask is constructed from a granular material with average grain diameter, w . The range of w that can be utilized for a given ghost-imaging resolution, ϕ , is limited. For $w \leq \phi$, contrast and resolution arise from the presence or absence of grains; insufficient contrast may result when $w \ll \phi$ or when grain packing is too dense. For $w > \phi$, the resolution is dictated by the sharpness of grain edges; however, $w \gg \phi$ would cause these edges to be sparse. The number of speckle positions required must increase accordingly.

The actual ghost-imaging experiment is shown in Fig. 2(b). Here, the previously known ensemble of illuminations $\{I_j(x, y)\}$ impinges upon a thin sample with intensity transmission function $T(x, y)$, where $0 \leq T(x, y) \leq 1$. Assuming unit efficiency for simplicity, the so-called bucket signal B_j measured by a large single-pixel detector for the j th illumination pattern is

$$B_j = \iint I_j(x, y) T(x, y) dx dy. \quad (1)$$

The ensemble of spatially random illumination patterns is assumed to obey spatial stationarity; stated differently, the intensity-intensity autocovariance of the illuminating speckle fields is, by assumption, well approximated by a function of coordinate differences. Equipped with this

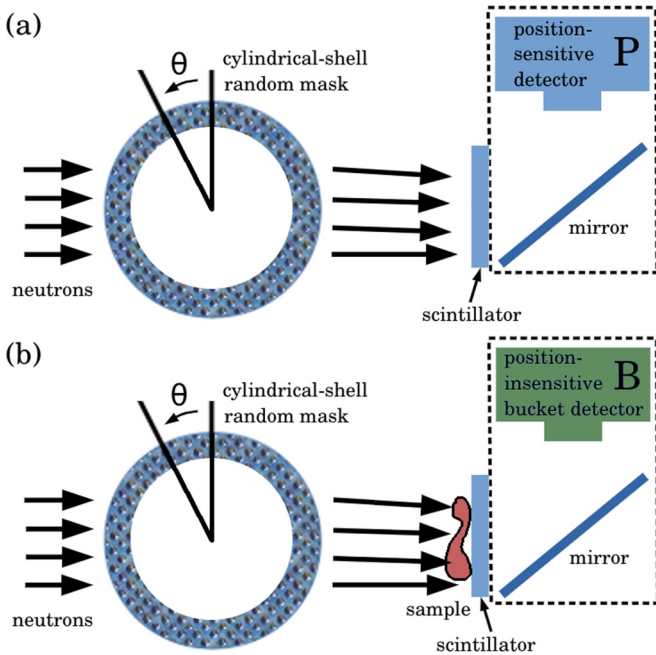


FIG. 2. Schematic for computational neutron ghost imaging. (a) Recording of spatially random illumination patterns, in the absence of a sample, using a position-sensitive detector P . Note that the scintillator converts a neutron-intensity distribution $f(x, y)$ that is incident upon it into a visible-light photon-intensity distribution $\xi f(x, y)$, where ξ is a suitable coupling constant that is proportional to the neutron-to-photon conversion efficiency. The intensity distribution of the scintillated photons is then diverted from the neutron beam path with a visible-light mirror, before entering the lens-plus-pixelated-detector camera system P , which directly images the photon-intensity distribution $\xi f(x, y)$ over the exit surface of the scintillator; this measured photon-intensity distribution is proportional to the neutron-intensity distribution that is incident upon the scintillator. (b) Recording of bucket signals, in the presence of a sample, using a position-insensitive lens-plus-photon-detector camera system detector (“bucket” detector B). The measured bucket signal is proportional to the integrated photon intensity over the exit surface of the scintillator, namely, $\iint \xi f(x, y) T(x, y) dx dy$, where $T(x, y)$ is the neutron-intensity transmission function for the sample. This integral is proportional to the integrated neutron intensity over the entrance surface of the scintillator.

enabling assumption, which implies that background-subtracted speckle fields may be considered to comprise a random basis for which distinct members are orthogonal in expectation value [48,49], the inverse problem [50,51] of computational ghost imaging then seeks to reconstruct $T(x, y)$ given $\{I_j(x, y), B_j\}$.

The cross-correlation (XC) method [9,11] approximates the sample’s transmission function via

$$T(x, y) \otimes \text{PSF}(x, y) \equiv \frac{1}{N} \sum_{j=1}^N (B_j - \bar{B}) I_j(x, y), \quad (2)$$

where $\bar{B} = E(B_j)$, E denotes expectation value, \otimes denotes two-dimensional convolution, and $\text{PSF}(x, y)$ is the effective

point spread function (PSF) associated with the ghost-imaging reconstruction [45,49]. This PSF is given by the previously mentioned autocovariance of the ensemble of speckle maps [45,52] (cf. Gordon *et al.* [26]):

$$\text{PSF}(x - x', y - y') = \frac{\mathcal{N}}{N} \sum_{j=1}^N I_j(x, y) I_j(x', y'). \quad (3)$$

Here, \mathcal{N} is a normalization constant chosen such that the PSF integrates to unity, and the assumption of spatial stationarity allows us to express the left side as a function of coordinate differences $(x - x', y - y')$. An improved estimate can be obtained by applying Landweber iteration [53] to the XC formula in Eq. (2) together with the associated forward model in Eq. (1), to give an iterative cross-correlation method (IXC) that has a narrower PSF. See Pelliccia *et al.* [45] and Kingston *et al.* [42,43], together with references therein, for details regarding IXC ghost imaging. The narrower PSF arising from IXC has the cost of increased reconstruction noise, which is the usual tradeoff between noise and spatial resolution [54]. IXC reconstructions may be improved via suitable regularization that incorporates constraints such as sparsity in image space, sparsity in image-gradient space, etc. [42,43].

III. EXPERIMENTAL METHODS

Experiments were performed using the open-pool reactor-based neutron source on the DINGO imaging beam line at the Australian Centre for Neutron Scattering (ACNS) [55,56]. An unfiltered polyenergetic neutron beam was employed, with a spectrum corresponding to thermal neutrons having maximum spectral intensity at wavelength 1.5 Å. The detector consisted of a ${}^6\text{LiF/ZnS:Cu}$ scintillation screen of thickness 50 μm , a mirror, and a Teledyne Photometrics Iris 15 sCMOS camera placed out of the neutron beam. The sCMOS camera has a 2960×5056 pixel array with a pixel pitch of 25.7 μm . The detector was positioned $L = 9.8$ m from a $d = 9.8$ mm pinhole at the neutron source, giving a beam divergence [57] of $\Theta = d/L = 1/1000$. A two-section 4.5-m-long flight tube filled with He at ambient pressure (1 bar) was used to reduce neutron scatter from air. In this configuration, the brightness of the neutron radiation was 9.0×10^6 n cm $^{-2}$ s $^{-1}$.

For this set of experiments, the rotation stage employed for tomography experiments on the DINGO beam line was used to vary the speckled illumination from the mask. Therefore, a cylindrical mask was employed, as depicted in Fig. 2. The cylindrical mask used for generating the speckle images was placed 150 mm upstream from the detector on an Aerotech ABRS 250 air-bearing rotation stage. Potential speckle-generating masks demonstrated to date have been formed from layers of granular materials such as metallic powders [58] and sand [59]; we note that foams (the inverse of grains) could also be used. The mask used here consisted of grains of iodized table salt (NaCl), with an average diameter of 1.3 mm. The salt grains were placed inside concentric aluminum cylinders with 1.0-mm-thick walls, an inner diameter of 40 mm, and an outer diameter of 60 mm. Note that the inner diameter is larger than the FOV used for the ghost-imaging

experiments (central 512×512 pixel region of the sCMOS camera). This ensures that the speckle properties (such as total transmission and magnification) are approximately constant so that the speckle images appear as two sets of granular layers translated in opposite directions.

Here we are performing computational ghost imaging, the first step of which is to record a set of high-quality images of the speckle illumination patterns produced by the salt grains. This step is depicted in Fig. 2(a). The mask was rotated to 1716 different positions, θ , with an angular increment of $\Delta\theta = 0.21$ degrees, and the set of illumination patterns generated was measured with 40 second exposure time. The second step is to record the bucket data, i.e., the total interaction (transmission in this case) of the object with each illumination pattern recorded in step 1. This step is depicted in Fig. 2(b). The object was placed in the beam in contact with the scintillation screen and the set of illumination patterns repeated from step 1. In this case, the bucket detector B was generated through software binning of data recorded with the same detector as in step 1, i.e., position sensitive detector P . In step 2, the set of mask positions was rapidly repeated with 5 second exposure time.

We present four experiments using two different objects. The first experiment demonstrates computational ghost imaging (CGI) with neutrons. The remaining three experiments explore the concept of parallelized CGI, where a contiguous array of ghost images is obtained. The two objects used for the experiments were as follows: (i) A cadmium (Cd) stencil constructed from a $400\text{-}\mu\text{m}$ -thick sheet of Cd with three holes drilled with diameters of 1.0, 3.0, and 5.0 mm. This stencil-like object was chosen on account of its simplicity, for the first experimental proof-of-concept neutron ghost image presented in our paper. (ii) A resolution star of diameter 20 mm with 128 radial lines of width 1.4 degrees created using laser ablation on a gadolinium (Gd) sputtered glass substrate [60]. The choice of a resolution star, for the second of two objects used in our experimental demonstration of neutron ghost imaging, demonstrates (i) the application of the method to a more complex sample, as well as (ii) enabling the resolution of the resulting reconstruction to be readily determined, e.g., via the smallest feature size in the resolution star that is resolved in the ghost-imaging reconstruction.

Neutron ghost imaging. The first experiment imaged the Cd stencil object and generated bucket measurements by software binning a 100×100 pixel subset of the recorded data to simulate a $2.57 \times 2.57 \text{ mm}^2$ bucket. The subset contained the 1.0 mm hole in the stencil.

Parallelized neutron-ghost imaging. The three parallelized neutron-ghost imaging experiments all interrogate a $13.2 \times 13.2 \text{ mm}^2$ FOV assuming position-sensitive detectors of decreasing pixel pitch as follows: 1.65, 0.822, and 0.411 mm. The FOV is then captured as 8×8 , 16×16 , and 32×32 pixel images (as is denoted later in Fig. 4). We consider each pixel as a bucket detector and refer to these low-resolution images as 2D arrays of bucket detectors. Parallelized neutron ghost imaging is achieved by performing ghost imaging on a per-pixel (or bucket-detector) basis. The second experiment again images the Cd stencil, while the last two experiments image a quadrant of the resolution star.

IV. RESULTS

The results will be presented in three sections. First, the speckle illumination patterns generated by the salt grain mask will be analyzed to determine the upper and lower limits to ghost-imaging resolution that can be expected. Second, computational ghost imaging (CGI) will be demonstrated with neutrons. Lastly, the proposed parallelized CGI method to enhance the resolution of images obtained by a conventional imaging detector, using CGI on a per-pixel basis, will be demonstrated.

A. Neutron speckle analysis

All experiments utilized the same prerecorded set of high-quality speckle illumination patterns for computational neutron ghost imaging and parallelized neutron ghost imaging. An example 100×100 pixel region of this speckled illumination is presented in Fig. 3(a). The contrast of these speckle images according to a form of Michelson visibility is $\kappa = 0.31$. The calculation adopted here was that of Eq. (57) in [47] that modified Michelson visibility to be less sensitive to extreme values, such as those from detected gamma rays in a neutron-imaging context; the equation is derived in footnote 3 of [47].

As outlined in the second paragraph of Sec. II, the potential resolution that one can recover in a ghost image, ϕ , is not necessarily directly determined by the grain size w of the speckle-generating mask. Here, $w \gg \phi$ and so ϕ depends on many factors of the experiment. We can expect ϕ to lie within a certain range, the limits of which are explained and determined as follows:

Based on the Shannon-Nyquist sampling theorem, the upper limit to ghost-imaging resolution in an ideal system is twice the pixel pitch of the speckle images: $51.4 \mu\text{m}$ in this case. However, this limit may not be reached if either (i) blur in the imaging system used to record the speckle patterns degrades resolution or (ii) the sharpness of the speckle generated by the mask does not attain this spatial frequency. A better estimate for the upper limit to resolution can be achieved by analyzing the resolution of the speckle images themselves. A common technique for estimating image resolution is that of Fourier ring correlation (FRC) [61]. Here the correlation of the information in two images is plotted as a function of spatial frequency. This has been presented as the blue curve in Fig. 3(b) for repeated measurements of the speckle presented in Fig. 3(a). The resolution is estimated as $0.004 \mu\text{m}^{-1}$. Adopting the Houston criterion [62] for resolution, this corresponds to a full width at half maximum (FWHM) of $250 \mu\text{m}$ and equates to a Gaussian PSF with a standard deviation of $100 \mu\text{m}$. The FRC result of a speckle image compared with itself blurred by this Gaussian function is presented as the red curve in Fig. 3(b) and displays similar resolution.

As previously mentioned, the lower limit to ghost-imaging resolution is well known to be characterized by the PSF generated by the autocovariance of the ensemble of speckle maps [7,15,52], as defined in Eq. (3). A profile through the PSF of the central pixel is presented as the green curve in Fig. 3(c). Again defining resolution as the FWHM of the PSF,

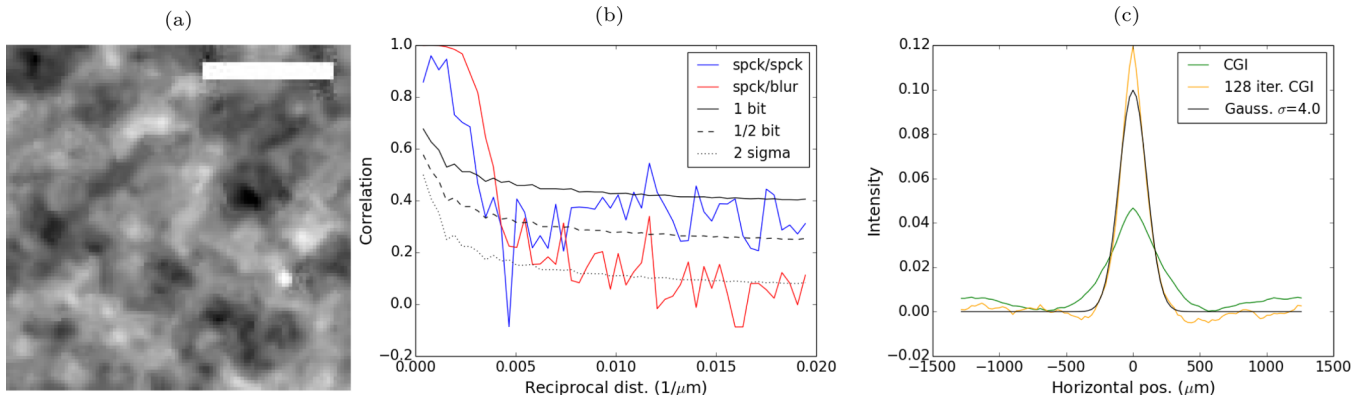


FIG. 3. (a) Example 100×100 pixel region of the speckle-intensity image generated by salt. 1.0 mm scale bar. (b) Speckle resolution analysis using Fourier ring correlation. Correlation of repeated measurements (blue plot, labeled spck/spck) contains a similar amount of information to a measurement correlated to itself after blurring by a Gaussian with a standard deviation of $100 \mu\text{m}$ (red plot, labeled spck/blur). (c) Profiles through the PSF generated by CGI (green) and 128 Landweber iterations of CGI (orange); cf. Gaussian function with a standard deviation of $100 \mu\text{m}$ (black).

this equates to $460 \mu\text{m}$ for the salt grains. Refining the PSF through the 128 Landweber iterations of the cross-correlation algorithm results in the orange profile shown in Fig. 3(c) and demonstrates that in the noise-free case, the upper limit to resolution from FRC analysis (black curve) can be attained. Therefore, we expect the resolution of our GI experiments, ϕ , to lie in the range $250 < \phi < 460 \mu\text{m}$.

B. Computational neutron ghost imaging

In order to demonstrate computational ghost imaging (CGI), the 1.0 mm hole drilled into the Cd stencil was imaged. A conventional image of the stencil blurred by a Gaussian PSF with a standard deviation of $100 \mu\text{m}$ is presented in Fig. 4(a-v). Given that 1716 speckle patterns and bucket values were collected, a ghost image of reasonable quality could be expected up to 42×42 pixels. However, being a stencil image, several strong priors could be asserted on the generated image that compensate for missing measurements. As a result, a 100×100 pixel ghost image was achievable. The results of image recovery by (a) conventional CGI, i.e., cross correlation, (b) 128 Landweber iterations of CGI, and (c) 128 regularized iterations of CGI (assuming sparsity in image-gradient space) are presented in Figs. 4(a-ii)–4(a-iv).

C. Parallelized computational neutron ghost imaging

Speckled illumination patterns of 512×512 pixels were recorded by conventional imaging with a $25.7 \mu\text{m}$ pixel pitch, i.e., FOV is 13.2 mm. Given the FRC results in Sec. IV A, that speckle illumination resolution $\phi = 250 \mu\text{m}$, these images were binned to 256×256 pixels with a $51.4 \mu\text{m}$ pixel pitch. Note that the lines at the boundary of the resolution star are spaced at $245 \mu\text{m}$ intervals, i.e., the resolution limit. We show three parallelized CGI scenarios given three different artificially spatially coarsened detectors with 1.65, 0.822, and 0.411 mm pixel pitch. We will demonstrate that the resolution of images from these coarse detectors can be enhanced to that of the speckle patterns (assumed to be known *a priori*) by treating each coarsened pixel as a bucket detector. Given the

higher-resolution speckle illumination patterns within each coarsened pixel (or bucket), we perform CGI per pixel to generate higher-resolution, finer-sampled images. It was shown in Sec. IV A that based on the speckle images recorded, we can expect to achieve a resolution of $250 < \phi < 460 \mu\text{m}$. We have therefore coarsened the speckled illumination patterns to have a pixel pitch of $51.4 \mu\text{m}$ and the parallelized CGI images will all be generated as 256×256 pixel arrays with a $51.4 \mu\text{m}$ pixel pitch.

Cadmium stencil. Here we assume a small 8×8 pixel camera with pixel pitch of 1.65 mm to cover the full 13.2 mm FOV. The object is the Cd stencil with 5.0, 3.0, and 1.0 mm holes; a conventional image of the object with this coarsened detector is given in Fig. 4(b-i). The object imaged with a high-resolution camera ($51.4 \mu\text{m}$ pixel pitch) blurred by a Gaussian function with a standard deviation of $100 \mu\text{m}$ is presented in Fig. 4(b-v). The results of parallelized neutron ghost imaging with a zoom factor of 32 recovered by (a) conventional CGI per bucket pixel, (b) 128 Landweber iterations of CGI per bucket pixel, and (c) 128 regularized iterations (assuming sparsity in image-gradient space) are presented in Figs. 4(b-ii)–4(b-iv).

Resolution star. The resolution star has been imaged under two scenarios: first, using a 16×16 pixel camera with pixel pitch of 0.822 mm to cover the full 13.2 mm FOV; second, using a 32×32 pixel camera with a 0.411 mm pixel pitch. Conventional images of the object with these coarsened detectors are given in Figs. 4(c-i) and 4(d-i). The object imaged with a high-resolution camera ($51.4 \mu\text{m}$ pixel pitch) blurred by a Gaussian function with a standard deviation of $100 \mu\text{m}$ is presented in Figs. 4(c-v) and 4(d-v). The results of parallelized neutron ghost imaging with zoom factors of 16 and 8, respectively, recovered by (a) conventional CGI per bucket pixel and (b) 128 Landweber iterations of CGI per bucket pixel, are presented in Figs. 4(c-ii)–4(c-iii) and 4(d-ii)–4(d-iii). Observe in these sets of images that artifacts arise on the boundaries of the bucket pixels. The ghost-imaging result is significantly improved after employing a Fourier filtering method (as demonstrated, e.g., in Fig. 13.39 of Hecht [63])

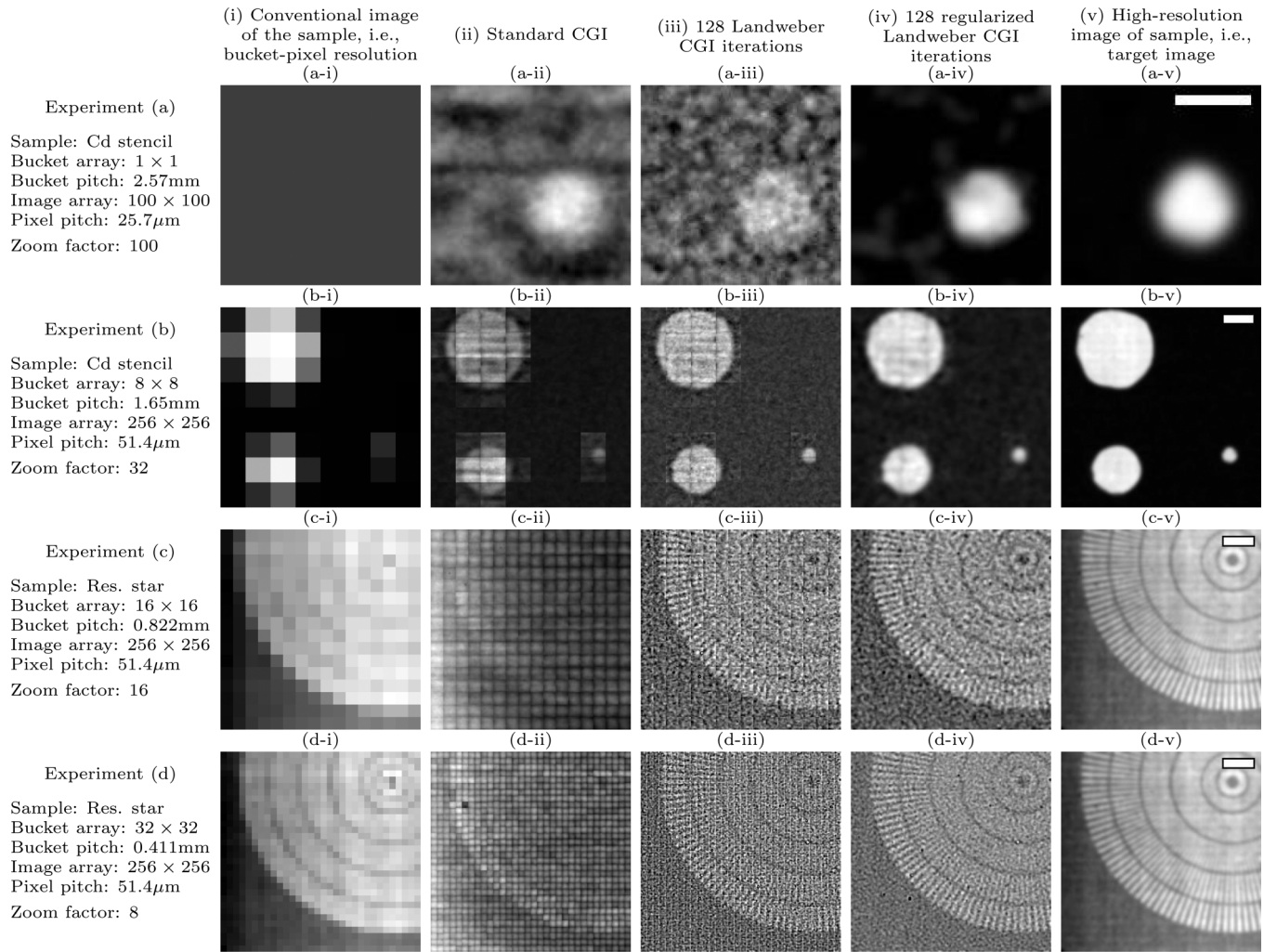


FIG. 4. Results for (a) neutron ghost imaging (1.0 mm scale bar) and (b)–(d) parallelized neutron ghost imaging (2.0 mm scale bar). The details for each experiment are given in the left panel. The data recorded for each experiment were collected with resolution as displayed in column (i) referred to as a *bucket array* with a pixel or *bucket pitch* as specified. In all cases, 1716 speckle-image and bucket-measurement pairs were used, with speckle images “prerecorded” or “known” at the specified image resolution. The results computed by various CGI methods (ii)–(iv) are all at the same resolution (that of the speckle images). However, they have required different *zoom factors* to achieve this (as specified). The right panel shows the samples imaged at this same resolution, providing the target image in each case. A single spatial scale bar for each row is given in the far-right column of images.

to suppress these bucket-pixel boundary artifacts during 128 regularized iterations of CGI (assuming image smoothness), as presented in Figs. 4(c-iv) and 4(d-iv).

V. DISCUSSION

Neutron computational ghost imaging (CGI) has been successfully demonstrated in Fig. 4(a) for a 1.0 mm hole in a Cd stencil. Observe that standard CGI by cross correlation (XC) in Fig. 4(a-ii) appears more faithful to the target image [Fig. 4(a-v)] than that from 128 Landweber iterations of XC (IXC) in Fig. 4(a-iii). This is true since a 100×100 pixel image has been computed from only 1716 speckle images. The speckle images form a basis for image representation [48,49] and 10 000 basis members are required for this image size, if they are orthogonal (more are required in this case). Regularization can compensate for this missing

information by using knowledge of the sample properties and making *a posteriori* assertions. This has been demonstrated in Fig. 4(a-iv) by assuming sparsity in image-gradient space.

Acquiring 1716 speckle images, and having an average speckle width of $w = 1.3$ mm, limits the total FOV that can be achieved by ghost imaging. However, this is perfectly suited to demonstrating parallelized neutron ghost imaging, replacing one large bucket detector with a small array of *bucket pixels*, each of which can be treated as a separate ghost-imaging experiment to yield a contiguous array of neutron ghost images. This resolution-enhancing concept has been demonstrated in the rows of Figs. 4(b)–4(d); the resolution of the object images has been improved from conventional imaging in column (i) through parallelized CGI to produce those in column (iv). For the Cd stencil experiment in Fig. 4(b), a dramatic improvement in resolution has been achieved. A zoom factor of 32 is possible since the stencil is the easiest

case for ghost imaging from an SNR perspective (as discussed in the following paragraph) as well as due to the possibility for more powerful *a posteriori* assertions in regularization. For the resolution star experiments, Fig. 4(c) shows a significant increase in resolution (zoom factor of 16), but to a lesser extent than the stencil; and Fig. 4(d) only has a zoom factor of 8, but demonstrates that the expected resolution [as shown in the target image in column (v)] can be achieved. We believe this demonstrates that the parallelized per-pixel CGI technique is a viable future avenue to overcome resolution limits imposed by neutron-detection difficulties and potentially resolve features below $10\ \mu\text{m}$.

We can show the advantage of stencils as ghost-imaging samples by considering the SNR of GI. The key point to observe is that SNR increases upon decreasing the number of nonzero elements in the sample transmission function [7,47]. It is for this reason that we chose, as the first of two objects imaged in our experimental proof of concept for neutron GI, a Cd stencil for which most of the sample area had neutron absorption close to 100%. In the high-brilliance limit, the SNR of the XC method in Eq. (2) is [47]

$$\text{SNR} = \kappa \sqrt{N/n_{\text{sample}}}. \quad (4)$$

Here, $\kappa \in [0, 1]$ is the Michelson visibility (i.e., the contrast) of the ensemble of illuminating speckle fields $\{I_j(x, y)\}$, and n_{sample} is the number of degrees of freedom for the sample transmission function. For a binary transmission function $T(x, y)$ that only takes the values of zero or unity, $n_{\text{sample}} = T_A/a$, where T_A is the area over which $T(x, y)$ is equal to unity, and a is the area occupied by the PSF (cf., e.g., Erkmen and Shapiro [7] and Pelliccia *et al.* [45]). Equation (4) quantifies the natural dependencies that (i) the SNR of a neutron ghost image is proportional to the contrast of the masks in the speckle fields from which it is additively composed via Eq. (2); (ii) the SNR is proportional to the square root of the number of utilized masks, a dependence that arises from the random-basis character [48,64] of the ensemble of illuminating speckle maps; (iii) for fixed κ and N , the SNR becomes lower as the number of degrees of freedom in $T(x, y)$ becomes larger, consistent with the observation that “stencil-like” transmission functions (namely, those for which $T_A/a \gg 1$) have relatively higher SNR in XC ghost-imaging reconstruction when compared to transmission functions for which $T_A/a \ll 1$.

With each bucket pixel zoomed in to 32×32 pixels in experiment (b) in Fig. 4, 1024 orthogonal speckle images are required for a complete basis. 1716 nonorthogonal, random speckle patterns were used and appear to be insufficient; however, regularization can compensate for this lack of information. Only 256 and 64 orthogonal speckle images are required for experiments (c) and (d), respectively, in Fig. 4. The same 1716 speckle patterns were used in these cases and therefore less regularization was required (only low-range image smoothness was assumed). This seemed to be approaching a sufficient set for experiment (d).

Observe that the standard CGI images obtained by XC [column (ii) in Fig. 4] for experiments (b)–(d) contained significant artifacts where the majority of the *bucket pixel* contains nonzero intensities; this is again related to the SNR

discussion in Sec. II. These issues are largely overcome by employing IXC [as demonstrated in column (iii)]. The most significant artifacts that remain are those related to bucket-pixel boundaries. These are commonly called *blocking artifacts* in image processing and are a common issue in super-resolution [65], image-tiling [63] and image-compression [66] contexts. For the Cd stencil results in Fig. 4(b), the heavy regularization that was possible largely overcame these artifacts; however, for the resolution star images, these had to be explicitly removed by Fourier filtering (as described in Sec. IV C) since less regularization was employed.

We close this discussion with some remarks regarding the spatial resolution of the method, ϕ . We have already seen that it is important to carefully distinguish between the following three length scales:

(i) *The size of the 3D grains in the speckle mask, w .* The grain width does not, in general, describe the length scale of features that are present in a speckle image. The characteristic transverse length scale of the speckles, at the exit surface of the mask, will typically be smaller than the grain diameter and will also be influenced by the sharpness of the mass-density gradients within each grain. High-resolution features in speckle images may arise from grain edges or from small regions of grain overlap.

(ii) *The spatial resolution (not pixel size) of the associated speckle images, as determined by FRC.* This describes the minimum feature size that can be measured by an individual speckle image. The GI resolution cannot exceed this limit: if spatial frequencies are not measured by any speckle pattern, they will not be present in the reconstruction. However, this resolution limit is not guaranteed to be reached due to factors such as poor-SNR measurements or insufficient recorded speckle patterns.

(iii) *The width of the PSF generated as the autocovariance of the speckle-image set [7,15,52].* The final resolution of the ghost-imaging reconstruction is limited by the number of, and any redundancy in, the full set of speckle patterns. Given a sufficient set of speckle images and high-fidelity measurements, it may be possible to exceed this resolution; however, this forms a lower limit on the resolution of the GI reconstruction.

These three characteristic length scales are of course related to one another, but they will in general be different in the numerical values that they take (and sometimes very different). Moreover, driven by the well-known trade-off between noise and spatial resolution [54], FRC resolution will also be influenced by noise in the detected images. Hence, resolution is a function of acquisition time, in addition to the dimensions and sharpness of the grains that comprise the speckle-generating mask. Further exploration of these interesting points, while beyond the scope of the present paper, would be an interesting avenue for further work.

VI. OTHER POTENTIAL FUTURE APPLICATIONS OF NEUTRON GHOST IMAGING

One of the strengths of the ghost-imaging (GI) concept is its ability to add spatial resolution to non-spatially resolving measurements. In other words, GI may be a viable alternative

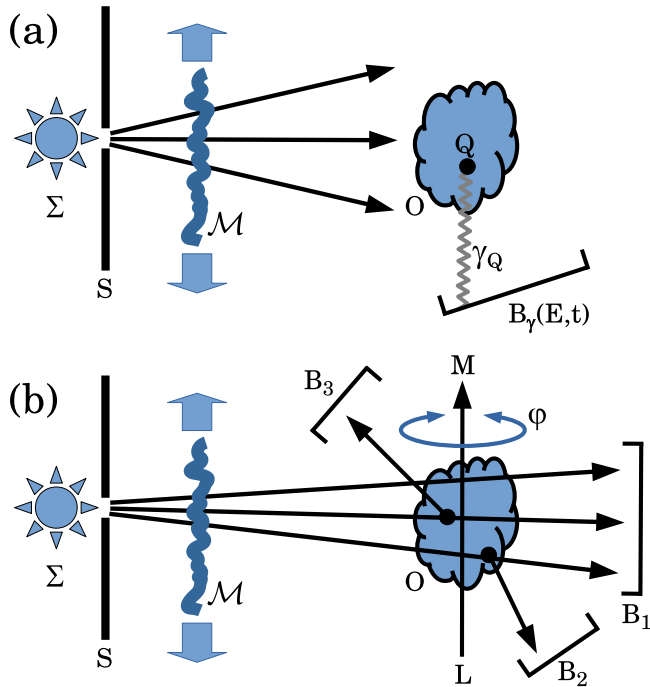


FIG. 5. (a) Setup for isotope-resolved neutron ghost imaging using prompt-gamma-ray detection. For each position of a well-characterized random mask \mathcal{M} , points such as Q within the object O may emit neutron-induced prompt-gamma radiation γ_Q to give a bucket signal $B_\gamma(E, t)$ that is measured using a gamma-ray spectrometer. This bucket signal may be measured as a function of both gamma-ray energy E and emission time t . (b) Setup for neutron ghost tomography, in which the object O may be rotated about the axis LM to a variety of azimuthal angles φ . Bucket B_1 may be used for bright-field neutron ghost tomography, while buckets B_2 and B_3 yield dark-field neutron ghost tomograms.

to conventional imaging in measurement situations where a pixel-array detector is not available or not practical.

One such technique is prompt-gamma neutron-activation analysis (PGAA), which measures the elemental composition of a sample through measuring the intensity and energy of prompt-gamma rays emitted by a sample that is irradiated by a neutron beam. Gamma spectrometers employed for these measurements could be multiplexed by a GI approach whereby the bucket signal $B_\gamma(E, t)$ measured by a gamma-ray spectrometer [see Fig. 5(a) for a depiction of this process] could be cross correlated with the illumination to produce a spatially resolved map of the elemental composition of the sample.

In ghost imaging, the problem of adding spatial resolution is shifted from the detector to the illumination beam, enabling one to use existing detector technology in a novel fashion. Note that in the spirit of the present work, the spatial resolution of such measurements could be tailored by adjusting the mask structure (and number of illuminations) so as to suit any specific neutron ghost-imaging experiment.

While the present paper has been devoted to neutron ghost imaging in two spatial dimensions, the penetrating power of neutrons enables the technique to be extended to 3D

neutron ghost imaging (“ghost tomography”), as recently accomplished with hard x rays [42,43]. In fact, complementing existing methods for bright-field [57] and dark-field [67] neutron tomography, one could devise the measurement scheme sketched in Fig. 5(b), whereby different bucket detectors acquire transmitted and scattered neutrons, while the mask displacement and the sample rotation permit multiple tomograms to be constructed using methods described in Kingston *et al.* [42,43].

The two examples given here are meant to illustrate some general guidelines towards augmenting existing neutron techniques with GI. We seek to inspire discussion around these topics, without going into the details of specific techniques. It is important to remark however, that mask design is a topic of intense research (see Higham *et al.* [68] for video-rate optical imaging, but also Kingston *et al.* [43] for work in hard x rays), which will greatly improve the ability to produce illumination masks that are optimized for the sample at hand. The imaging problem is thus recast in terms of beam shaping—avoiding building complexity into the detector design—and computational algorithms, in the spirit of what is broadly described as computational imaging: a hybrid hardware-software imaging system [69], able to overcome limitations of optics and pixel-array detector systems.

VII. CONCLUSION

A protocol for computational neutron ghost imaging was outlined and applied to two separate experiments. The first achieved computational neutron ghost imaging by illuminating a sample with an ensemble of spatially random neutron fields and subsequently registering the total sample transmission using a single bucket detector. This enables position resolution to be incorporated into a variety of neutron-scattering instruments, which do not currently possess imaging capability. The second experiment demonstrated a parallelized form of neutron ghost imaging. Here, a ghost image was independently reconstructed for each pixel of a detector with artificially coarsened spatial resolution, thereby demonstrating the principle that parallelized neutron ghost imaging can be used in the future to increase the effective spatial resolution of the detector. Avenues for future work include tomographic neutron ghost imaging, dark-field neutron ghost imaging, and isotope-resolved color neutron ghost imaging via prompt-gamma-ray bucket detection.

ACKNOWLEDGMENTS

A.M.K. and G.R.M. acknowledge the financial support of the Australian Research Council and FEI-Thermo Fisher Scientific through Linkage Project No. LP150101040, and the use of supercomputer time provided by Australia’s National Computational Infrastructure (NCI). D.P., D.M.P., and G.R.M. acknowledge travel support from the Australian Nuclear Science and Technology Organisation. The authors acknowledge useful discussions with Jeremy Brown, Margaret Elcombe, Wilfred Fullagar, Tim Petersen, Kirrily Rule, Adrian Sheppard, Anton Stampfl, Andrew Studer, and Imants Svalbe.

- [1] D. N. Klyshko, Effect of focusing on photon correlation in parametric light scattering, *Sov. Phys. JETP* **67**, 1131 (1988).
- [2] A. V. Belinskii and D. N. Klyshko, Two-photon optics: Diffraction, holography, and transformation of two-dimensional signals, *Sov. Phys. JETP* **78**, 259 (1994).
- [3] T. B. Pittman, Y. H. Shih, D. V. Strekalov, and A. V. Sergienko, Optical imaging by means of two-photon quantum entanglement, *Phys. Rev. A* **52**, R3429 (1995).
- [4] D. V. Strekalov, A. V. Sergienko, D. N. Klyshko, and Y. H. Shih, Observation of Two-Photon ‘Ghost’ Interference and Diffraction, *Phys. Rev. Lett.* **74**, 3600 (1995).
- [5] R. S. Bennink, S. J. Bentley, and R. W. Boyd, ‘Two-Photon’ Coincidence Imaging with a Classical Source, *Phys. Rev. Lett.* **89**, 113601 (2002).
- [6] B. I. Erkmén and J. H. Shapiro, Unified theory of ghost imaging with Gaussian-state light, *Phys. Rev. A* **77**, 043809 (2008).
- [7] B. I. Erkmén and J. H. Shapiro, Ghost imaging: From quantum to classical to computational, *Adv. Opt. Photon.* **2**, 405 (2010).
- [8] T. J. Lane and D. Ratner, What are the advantages of ghost imaging? Multiplexing for x-ray and electron imaging, *Opt. Express* **28**, 5898 (2020).
- [9] O. Katz, Y. Bromberg, and Y. Silberberg, Compressive ghost imaging, *Appl. Phys. Lett.* **95**, 131110 (2009).
- [10] R. I. Stantchev, B. Sun, S. M. Hornett, P. A. Hobson, G. M. Gibson, M. J. Padgett, and E. Hendry, Noninvasive, near-field terahertz imaging of hidden objects using a single-pixel detector, *Sci. Adv.* **2**, e1600190 (2016).
- [11] Y. Bromberg, O. Katz, and Y. Silberberg, Ghost imaging with a single detector, *Phys. Rev. A* **79**, 053840 (2009).
- [12] R. Hanbury Brown and R. Twiss, Correlation between photons in two coherent beams of light, *Nature (London)* **177**, 27 (1956).
- [13] R. Hanbury Brown and R. Twiss, A test of a new type of stellar interferometer on Sirius, *Nature (London)* **178**, 1046 (1956).
- [14] L. G. Wang, S. Qamar, S.-Y. Zhu, and M. S. Zubairy, Hanbury Brown–Twiss effect and thermal light ghost imaging: A unified approach, *Phys. Rev. A* **79**, 033835 (2009).
- [15] J. H. Shapiro, Computational ghost imaging, *Phys. Rev. A* **78**, 061802(R) (2008).
- [16] M. F. Duarte, M. A. Davenport, D. Takbar, J. N. Laska, T. Sun, K. F. Kelly, and R. G. Baraniuk, Single-pixel imaging via compressive sampling, *IEEE Signal Process. Mag.* **25**, 83 (2008).
- [17] M.-J. Sun, M. P. Edgar, G. M. Gibson, B. Sun, N. Radwell, R. Lamb, and M. J. Padgett, Single-pixel three-dimensional imaging with time-based depth resolution, *Nat. Commun.* **7**, 12010 (2016).
- [18] J. H. Shapiro and R. W. Boyd, The physics of ghost imaging, *Quant. Info. Proc.* **11**, 949 (2012).
- [19] M. J. Padgett and R. W. Boyd, An introduction to ghost imaging: Quantum and classical, *Philos. Trans. R. Soc. A* **375**, 20160233 (2017).
- [20] H. Yu, R. Lu, S. Han, H. Xie, G. Du, T. Xiao, and D. Zhu, Fourier-Transform Ghost Imaging with Hard X Rays, *Phys. Rev. Lett.* **117**, 113901 (2016).
- [21] D. Pelliccia, A. Rack, M. Scheel, V. Cantelli, and D. M. Paganin, Experimental X-Ray Ghost Imaging, *Phys. Rev. Lett.* **117**, 113902 (2016).
- [22] A. Schori and S. Schwartz, X-ray ghost imaging with a laboratory source, *Opt. Express* **25**, 14822 (2017).
- [23] R. I. Khakimov, B. M. Henson, D. K. Shin, S. S. Hodgman, R. G. Dall, K. G. H. Baldwin, and A. G. Truscott, Ghost imaging with atoms, *Nature (London)* **540**, 100 (2017).
- [24] S. S. Hodgman, W. Bu, S. B. Mann, R. I. Khakimov, and A. G. Truscott, Higher-Order Quantum Ghost Imaging with Ultracold Atoms, *Phys. Rev. Lett.* **122**, 233601 (2019).
- [25] S. Li, F. Cropp, K. Kabra, T. J. Lane, G. Wetzstein, P. Musumeci, and D. Ratner, Electron Ghost Imaging, *Phys. Rev. Lett.* **121**, 114801 (2018).
- [26] J. Gordon, N. Kroó, G. Orbán, L. Pál, P. Pellionisz, F. Szlávik, and I. Vizi, Correlation Type Time-Of-Flight Spectrometer with Magnetically Pulsed Polarized Neutrons, *Phys. Lett. A* **26**, 122 (1968).
- [27] K. Sköld, A mechanical correlation chopper for thermal neutron spectroscopy, *Nucl. Instrum. Methods* **63**, 114 (1968).
- [28] R. Von Jan and R. Scherm, The statistical chopper for neutron time-of-flight spectroscopy, *Nucl. Instrum. Methods* **80**, 69 (1970).
- [29] G. Wilhelmi and F. Gompf, Binary sequences and error analysis for pseudo-statistical neutron modulators with different duty cycles, *Nucl. Instrum. Methods* **81**, 36 (1970).
- [30] D. L. Price and K. Sköld, A detailed evaluation of the mechanical correlation chopper for neutron time-of-flight spectrometry, *Nucl. Instrum. Methods* **82**, 208 (1970).
- [31] L. D. Cussen, J. C. Osborn, P. Gibbs, and T. J. Hicks, The use of a pseudo-random spin flipper sequence on a polarised neutron scattering instrument, *Nucl. Instrum. Methods Phys. Res. A* **314**, 155 (1992).
- [32] K. Chen and S. Han, Microscopy for atomic and magnetic structures based on thermal neutron Fourier-transform ghost imaging, [arXiv:1801.10046](https://arxiv.org/abs/1801.10046).
- [33] *Neutron Imaging and Applications: A Reference for the Imaging Community*, edited by H. Z. Bilheux, R. McGreevy, and I. S. Anderson (Springer, Boston, 2009).
- [34] J. T. Cremer, Jr., X-ray and neutron optics, *Adv. Imag. Elect. Phys.* **172**, 607 (2012).
- [35] P. Trtik, J. Hovind, C. Grünzweig, A. Bollhalder, V. Thominet, C. David, A. Kaestner, and E. H. Lehmann, Improving the spatial resolution of neutron imaging at Paul Scherrer Institut—The neutron microscope project, *Phys. Procedia* **69**, 169 (2015).
- [36] P. Trtik and E. H. Lehmann, Isotopically-enriched gadolinium-157 oxysulfide scintillator screens for the high-resolution neutron imaging, *Nucl. Instrum. Methods Phys. Res. A* **788**, 67 (2015).
- [37] P. Herrmann, K. A. Steinhauser, R. Gähler, A. Steyerl, and W. Mampe, Neutron Microscope, *Phys. Rev. Lett.* **54**, 1969 (1985).
- [38] H. R. Beguiristain, I. S. Anderson, C. D. Dewhurst, M. A. Piestrup, J. T. Cremer, and R. H. Pantell, A simple neutron microscope using a compound refractive lens, *Appl. Phys. Lett.* **81**, 4290 (2002).
- [39] M. R. Eskildsen, P. L. Gammel, E. D. Isaacs, C. Detlefs, K. Mortensen, and D. J. Bishop, Compound refractive optics for the imaging and focusing of low-energy neutrons, *Nature (London)* **391**, 563 (1998).
- [40] H. Leemreize, E. B. Knudsen, J. O. Birk, M. Strobl, C. Detlefs, and H. F. Poulsen, Full-field neutron microscopy based on refractive optics, *J. Appl. Crystallogr.* **52**, 1299 (2019).
- [41] M. Utsuro and V. K. Ignatovich, *Handbook of Neutron Optics* (Wiley VCH Verlag GmbH, Weinheim, 2010).

- [42] A. M. Kingston, D. Pelliccia, A. Rack, M. P. Olbinado, Y. Cheng, G. R. Myers, and D. M. Paganin, Ghost tomography, *Optica* **5**, 1516 (2018).
- [43] A. M. Kingston, G. R. Myers, D. Pelliccia, I. D. Svalbe, and D. M. Paganin, X-ray ghost-tomography: Artefacts, dose distribution, and mask considerations, *IEEE Trans. Comput. Imag.* **5**, 136 (2019).
- [44] A.-X. Zhang, Y.-H. He, L.-A. Wu, L.-M. Chen, and B.-B. Wang, Table-top x-ray ghost imaging with ultra-low radiation, *Optica* **5**, 374 (2018).
- [45] D. Pelliccia, M. P. Olbinado, A. Rack, A. M. Kingston, G. R. Myers, and D. M. Paganin, Towards a practical implementation of x-ray ghost imaging with synchrotron light, *IUCrJ* **5**, 428 (2018).
- [46] Here, and throughout the paper, “thin” is taken to be synonymous with “optically thin” in the sense that the projection approximation [70] may be assumed to hold, at the level of intensity. Stated differently, when illuminated by neutrons that are paraxial with respect to the optical axis z , the neutron intensity in the presence of a “thin” object over a planar exit surface perpendicular to the optical axis is, by assumption, well approximated by the product of (i) the illumination intensity over the sample’s entrance surface and (ii) an intensity transmission function that is a function of transverse coordinates.
- [47] D. M. Paganin, Writing arbitrary distributions of radiant exposure by scanning a single illuminated spatially random screen, *Phys. Rev. A* **100**, 063823 (2019).
- [48] D. Ceddia and D. M. Paganin, Random-matrix bases, ghost imaging, and x-ray phase contrast computational ghost imaging, *Phys. Rev. A* **97**, 062119 (2018).
- [49] T. E. Gureyev, D. M. Paganin, A. Kozlov, Ya. I. Nesterets, and H. M. Quiney, Complementary aspects of spatial resolution and signal-to-noise ratio in computational imaging, *Phys. Rev. A* **97**, 053819 (2018).
- [50] P. C. Sabatier, Modelling or solving inverse problems? in *Inverse Methods in Action*, edited by P. C. Sabatier (Springer, Berlin, 1990), pp. 1–14.
- [51] P. C. Sabatier, Past and future of inverse problems, *J. Math. Phys.* **41**, 4082 (2000).
- [52] F. Ferri, D. Magatti, L. A. Lugiato, and A. Gatti, Differential Ghost Imaging, *Phys. Rev. Lett.* **104**, 253603 (2010).
- [53] L. Landweber, An iteration formula for Fredholm integral equations of the first kind, *Am. J. Math.* **73**, 615 (1951).
- [54] T. E. Gureyev, Ya. I. Nesterets, F. de Hoog, G. Schmalz, S. C. Mayo, S. Mohammadi, and G. Tromba, Duality between noise and spatial resolution in linear systems, *Opt. Express* **22**, 9087 (2014).
- [55] U. Garbe, T. Randall, C. Hughes, G. Davidson, S. Pangelis, and S. J. Kennedy, A new neutron radiography/tomography/imaging station DINGO at OPAL, *Phys. Proc.* **69**, 27 (2015).
- [56] U. Garbe, Y. Ahuja, R. Ibrahim, H. Li, L. Aldridge, F. Salvemini, and A. Z. Paradowska, Industrial application experiments on the neutron imaging instrument DINGO, *Phys. Proc.* **88**, 13 (2017).
- [57] W. Treimer, Neutron tomography, in *Neutron Imaging and Applications: A Reference for the Imaging Community*, edited by H. Z. Bilheux, R. McGreevy, and I. S. Anderson (Springer US, Boston, 2009), pp. 81–108.
- [58] G. Song, J. Y. Y. Lin, J. C. Bilheux, Q. Xie, L. J. Santodonato, J. J. Molaison, H. D. Skorpenske, A. M. Dos Santos, C. A. Tulk, K. An, A. D. Stoica, M. M. Kirka, R. R. Dehoff, A. S. Tremsin, J. Bunn, L. M. Sochalski-Kolbus, and H. Z. Bilheux, Characterization of crystallographic structures using Bragg-edge neutron imaging at the spallation neutron source, *J. Imag.* **3**, 65 (2017).
- [59] F. H. Kim, D. Penumadu, J. Gregor, N. Kardjilov, and I. Manke, High-resolution neutron and x-ray imaging of granular materials, *J. Geotech. Geoenviron. Eng.* **139**, 715 (2013).
- [60] C. Grünzweig, G. Frei, E. Lehmann, G. Kühne, and C. David, Highly absorbing gadolinium test device to characterize the performance of neutron imaging detector systems, *Rev. Sci. Instrum.* **78**, 053708 (2007).
- [61] M. Van Heel, Similarity measures between images, *Ultramicroscopy* **21**, 95 (1987).
- [62] W. V. Houston, The fine structure and the wave-length of the Balmer lines, *Astrophys. J.* **64**, 81 (1926).
- [63] E. Hecht, *Optics*, 5th ed. (Pearson Education, Essex, 2017).
- [64] A. N. Gorban, I. Y. Tyukin, D. V. Prokhorov, and K. I. Sofeikov, Approximation with random bases: Pro et contra, *Inf. Sci.* **364**, 129 (2016).
- [65] J. D. Van Ouwerkerk, Image super-resolution survey, *Image Vision Comput.* **24**, 1039 (2006).
- [66] H. C. Reeve and J. S. Lim, Reduction of blocking effects in image coding, *Opt. Eng.* **23**, 34 (1984).
- [67] M. Strobl, C. Grünzweig, A. Hilger, I. Manke, N. Kardjilov, C. David, and F. Pfeiffer, Neutron Dark-Field Tomography, *Phys. Rev. Lett.* **101**, 123902 (2008).
- [68] C. F. Higham, R. Murray-Smith, M. J. Padgett, and M. P. Edgar, Deep learning for real-time single-pixel video, *Sci. Rep.* **8**, 2369 (2018).
- [69] D. Paganin, T. E. Gureyev, S. C. Mayo, A. W. Stevenson, Y. I. Nesterets, and S. W. Wilkins, X-ray omni microscopy, *J. Microsc.* **214**, 315 (2004).
- [70] D. M. Paganin, *Coherent X-Ray Optics* (Oxford University Press, Oxford, 2006).